The algorithm of microphysical parameter profiles of aerosol and small cloud droplets based on the dual wavelength Lidar data

Huige Di, Xinhong Wang, Ning Chen, Jing Guo, Wenhui Xin, Shichun Li, Yan Guo, Qing Yan, Yufeng Wang, Dengxin Hua*

School of Mechanical and Precision Instrument Engineering, Xi'an University of Technology, Xi'an 710048, China

Correspondence to: Dengxin Hua (dengxinhua@xaut.edu.cn)

Abstract. This study proposed an inversion method of atmosphere aerosol or cloud microphysical parameters based on dual wavelength lidar data. The matching characteristics between aerosol/cloud particle size distribution and Gamma distribution were studied using aircraft observation data. The feasibility of particle effective radius retrieval from lidar ratio and backscatter ratio was simulated and studied. A method for inverting the effective radius and number concentration of atmospheric aerosols or small cloud droplets using backscatter ratio was proposed, and the error sources and applicability of the algorithm were analyzed. This algorithm was suitable for the inversion of uniformly mixed and single property aerosol layers or small cloud droplets. Compared with the previous study, this algorithm could quickly obtain the microphysical parameters of atmosphere particles and has good robustness. For aerosol particles, the inversion range that this algorithm can achieve was 0.3-1.7 μm. For cloud droplets, it was 1.0-10 μm. An atmosphere observation experiment was conducted using the multi-wavelength lidar developed by Xi'an University of Technology, and a thin cloud formation process was captured. The microphysical parameters of aerosol and cloud during this process were retrieved. The results clearly demonstrate the growth of effective radius and number concentration.

Key words: Lidar; Effective radius; Gamma distribution; Aerosol; Cloud

1 Intruction

The vertical characteristics of aerosol and cloud are of great significance for the study of many scientific issues, such as the interaction between aerosol and cloud, the mechanism of atmospheric pollution generation, and so on (Lohmann and Feichter, 2005; Kulmala et al., 2004; Miffre et al., 2010). The high-precision detection of aerosol and cloud microphysical parameters at vertical altitude is important. At present, the main methods for obtaining atmosphere aerosol or cloud microphysical parameters include in-situ observation (He et al., 2019; Moore et al., 2021; Gao et al., 2022a; Gao et al., 2022b) and remote sensing observation (Vivekanandan et al., 2020; Johnson et al., 2009). People can obtain microphysical parameters of cloud or aerosol at vertical altitudes by mounting in-situ observation instruments on equipment such as airplanes or balloons (Kaufman et al., 1998; Cai et al., 2022), but this method has a low detection frequency and cannot obtain continuous observation data with high temporal and spatial resolution (Zhao et al., 2018). Lidar, with its advantages of high temporal and spatial resolution and high detection sensitivity, has been widely used in the field of atmosphere detection, and has important application potential in detecting optical an5bd microphysical parameters of atmosphere aerosol and cloud (Vivekanandan et al., 2020; Hara et al., 2018; Siomos et al., 2017; Kanitz et al., 2013; Dionisi et al., 2018).

The remote sensing detection of aerosol or cloud microphysical parameters mainly uses three wavelength lidar, which can obtain four or more optical parameters (usually requiring two extinction coefficients @355 nm&532 nm and three backscatter coefficients @ 355 nm&532 nm&1064 nm) for the retrieval of aerosol microphysical parameters (Veselovskii et al., 2004; Müller et al., 1999; Veselovskii et al., 2009). The regularization algorithm (Kolgotin et al., 2023; Veselovskii et al., 2002), the principal component analysis (PCA) technique (Martin et al., 2013), and the linear estimation algorithm (Veselovskii et al., 2012) have been used for determining the aerosol bulk properties. These algorithms do not require the assumption of complex refractive index or aerosol particle size distribution (APSD), so they have been widely studied, but their applications are limited. The inversion results are unstable, and there will be good results under certain spectral types; however, in some cases, the

41 inversion error is very large. Not only that, the above methods require the complex lidar hardware systems (Di et al., 2018a;
42 Meskhidze et al., 2021; Müller et al., 2014). Therefore, the above algorithms cannot be well applied in most lidar systems
43 (most lidars in AERONET are dual wavelength), and it is necessary to establish a more reasonable method for inverting
44 microphysical parameters.

45 This study proposes an inversion method of atmosphere aerosol or cloud microphysical parameters based on dual
46 wavelength Lidar. This article mainly includes the following parts: in Section 2, we studied the APSD and cloud droplet size
47 distribution (CDSD) measured by airborne instruments and found that they are basically consistent with the Gamma
48 distribution, and extract the statistical characteristics of their Gamma distribution parameters; In Section 3, the inversion
49 method and simulation analysis results were presented and described; In Section 4, an atmosphere observation result by lidar
50 was presented; Section 5 is the conclusion and discussion.

51 **2 Gamma distribution statistical characteristics of APSD and CDSD**

52 **2.1 Gamma distribution**

53 The particle size distribution (Di et al., 2018a) is the variation of particle number with particle radius within a certain
54 radius range $r \sim r + dr$ per unit volume, defined as

55
$$n(r) = \frac{dN}{dr} \tag{1}$$

56 here, r is the particle radius, $n(r)$ is the particle size distribution, N is the total number of particles per unit volume. The effective
57 radius (Di et al., 2018a) is an important parameter that characterizes the average particle size, defined as the ratio of the third-
58 order and second-order moments of the particle size distribution, as shown below

59
$$r_{\text{eff}} = \frac{\int_{r_{\min}}^{r_{\max}} r^3 n(r) dr}{\int_{r_{\min}}^{r_{\max}} r^2 n(r) dr} \tag{2}$$

60 The most common models for APSD are Junge distribution and lognormal distribution. CDSD usually described as Gamma
61 distribution or corrected Gamma distribution (Kolgotin et al., 2023). The Gamma function has the advantages of integrability
62 and recursion of various order functions. In this paper, the Gamma distribution is used to describe APSD and CDSD. In
63 mathematics, $\Gamma(x)$ is defined as Gamma function, and is as follow

64
$$\Gamma(x) = \int_0^{+\infty} t^{x-1} e^{-t} dt \, , \, (x>0) \tag{3}$$

65 Then, the particle size distribution can be written as

66
$$n(r) dr = a r^b e^{-cr} dr \tag{4}$$

67 here, a is related to particle concentration, b is a dimensionless parameter representing shape factor, which is related to
68 spectral width, and c is a slope parameter. Its p-th moment can be expressed as

69
$$M_p = \int_{r_{\min}}^{r_{\max}} r^p n(r) dr = \int_{r_{\min}}^{r_{\max}} r^p a r^b e^{-cr} dr = \frac{a}{c^{p+b+1}} \Gamma(p+b+1) \tag{5}$$

70 The effective radius requires second-order and third-order moments, which are

71
$$M_2 = \int_{r_{\min}}^{r_{\max}} r^2 n(r) dr = \frac{a}{c^{2+b+1}} \Gamma(2+b+1) \tag{6}$$

72
$$M_3 = \int_{r_{\min}}^{r_{\max}} r^3 n(r) dr = \frac{a}{c^{3+b+1}} \Gamma(3+b+1) \tag{7}$$

73 Substituting Eq. (6) and Eq. (7) into Eq. (2) yields the effective radius as follow

74
$$r_{\text{eff}} = \frac{M_3}{M_2} = \frac{\int_{r_{\min}}^{r_{\max}} r^3 n(r)\mathrm{d}r}{\int_{r_{\min}}^{r_{\max}} r^2 n(r)\mathrm{d}r} = \frac{1}{c}\frac{\Gamma(3+b+1)}{\Gamma(2+b+1)} \tag{8}$$

75   The Gamma function has recursion, as shown in the following formula

76
$$\Gamma(x+1) = x\Gamma(x) \tag{9}$$

77   According to Eq. (8) and Eq. (9), the effective radius can be simplified as

78
$$r_{\text{eff}} = \frac{b+3}{c} \tag{10}$$

79   **2.2 APSDs and CDSDs in the vertical altitude**

80   In order to study the characteristics of APSDs and CDSDs in the vertical altitude, the APSDs and CDSDs obtained from
81   aircraft observations by the Hebei Provincial Weather Modification Office were analyzed (from 2005 to 2006). APSDs were
82   measured by the PCASP-100X probe, and CDSDs were obtained by the FSSP-100-ER probe (Di et al., 2018b). The number
83   concentration, effective radius and optical parameter profiles were calculated based on those APSDs and CDSDs. Fit the
84   obtained APSDs and CDSDs one by one using Gamma function, and statistically analyze these fitting parameters. ~3500 sets
85   of APSDs and 2221 sets of CDSDs were statistically analyzed. Over 95% of the data have a high goodness of fit in the Gamma
86   distribution. The goodness of fit of CDSDs is higher than that of APSDs, with CDSDs of 0.983 and APSDs of 0.856. The
87   parameter a of CDSDs are significantly larger than that of APSDs, and there are obvious differences of b and c for cloud and
88   aerosol. The literature suggests that there is a certain functional relationship between the Gamma parameters b and c of CDSDs
89   (Ding et al., 2023). Statistical analysis was conducted on the *b* and *c* parameters of APSDs and CDSDs, as shown in Fig. 1.
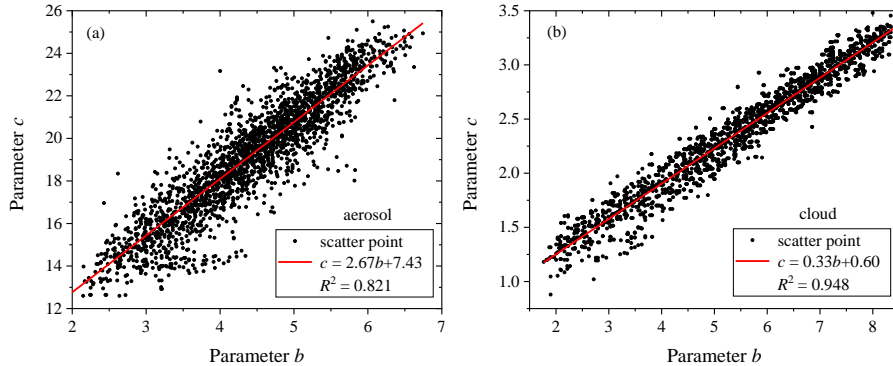
90
91   **Figure 1.** Statistical Results of parameter *b* and *c* in aerial survey data. (a)Aerosol particles, (b)cloud droplets.

92   According to Fig. 1, there are the remarkable linear relationships between parameter *b* and *c*. The fitting functions for
93   CDSDs and APSDs are as follows

94
$$\begin{cases} c_{\text{cloud}} = 0.33b_{\text{cloud}} + 0.60 \\ c_{\text{aerosol}} = 2.67b_{\text{aerosol}} + 7.43 \end{cases} \tag{11}$$

95   The linear relationship between the two parameters of CDSDs is better with a goodness of fit of 0.948, and a linear goodness
96   of fit of 0.821 for APSDs. According to the statistical results, the parameter *b* of APSDs at vertical height is mainly distributed
97   in the range of 2-7, and CDSDs is mainly distributed in the range of 2-8.

98   **3. The Inversion method for microphysical parameters of atmosphere aerosols or small cloud droplets**

99   **3.1 Inversion algorithm**

100   The first step in this algorithm is the retrieval of the effective radius. The parameter *a* in Gamma distribution shown in Eq.
101   (4) is related to number concentration. The ratio $O_R(m, r)$ (lidar ratio or color ratio) of the two optical parameters can eliminate

102 parameter a, and can be written as

$$O_R(m,r) = \frac{g_1(\lambda_1)}{g_2(\lambda_2)} \tag{12}$$

104 here, m is the complex refractive index of particles, $g_1(\lambda_1)$ and $g_2(\lambda_2)$ are the optical parameters at two wavelengths λ_1 and λ_2,

105 respectively. It can also be written as follows

$$O_R(m,r) = \frac{\int_{r_{\min}}^{r_{\max}} \pi r^2 Q_1(m,r,\lambda_1) r^b e^{-cr} \, \mathrm{d}r}{\int_{r_{\min}}^{r_{\max}} \pi r^2 Q_2(m,r,\lambda_2) r^b e^{-cr} \, \mathrm{d}r} \tag{13}$$

107 where Q_1 and Q_2 are the extinction efficiency factor or backscattering efficiency factor at λ_1 and λ_2. Using the effective radius

108 in the Eq. (10) instead of parameter c, the Eq. (13) can be written as follows

$$O_R(m,r_{\mathrm{eff}}) = \frac{\int_{r_{\min}}^{r_{\max}} \pi r^2 Q_1(m,r,\lambda_1) r^b e^{-\frac{b+3}{r_{\mathrm{eff}}}r} \, \mathrm{d}r}{\int_{r_{\min}}^{r_{\max}} \pi r^2 Q_2(m,r,\lambda_2) r^b e^{-\frac{b+3}{r_{\mathrm{eff}}}r} \, \mathrm{d}r} \tag{14}$$

110 According to the Eq. (11) and Eq. (14), if the ratio of optical parameters monotonically changes with the effective radius, the

111 effective radius can be obtained from the ratio of optical parameters, and then parameters b and c can also be obtained according

112 to Eq. (11). The ratio here can be chosen as the ratio of backscatter or extinction coefficient of two wavelengths (color ratio)

113 or the ratio of extinction coefficient of one wavelength to backscatter coefficient (lidar ratio).

114 After obtaining b and c, a can be derived from the Eq. (15), written as

$$a = \frac{\int_{r_{\min}}^{r_{\max}} \pi r^2 Q_1(m,r,\lambda_1) a r^b e^{-cr} \, \mathrm{d}r}{\int_{r_{\min}}^{r_{\max}} \pi r^2 Q_1(m,r,\lambda_1) r^b e^{-cr} \, \mathrm{d}r} = \frac{g_1(\lambda_1)}{\int_{r_{\min}}^{r_{\max}} \pi r^2 Q_1(m,r,\lambda_1) r^b e^{-cr} \, \mathrm{d}r} \tag{15}$$

116 and then, the number concentration N can be calculated by integrating the Eq. (4). The algorithm flowchart is shown below
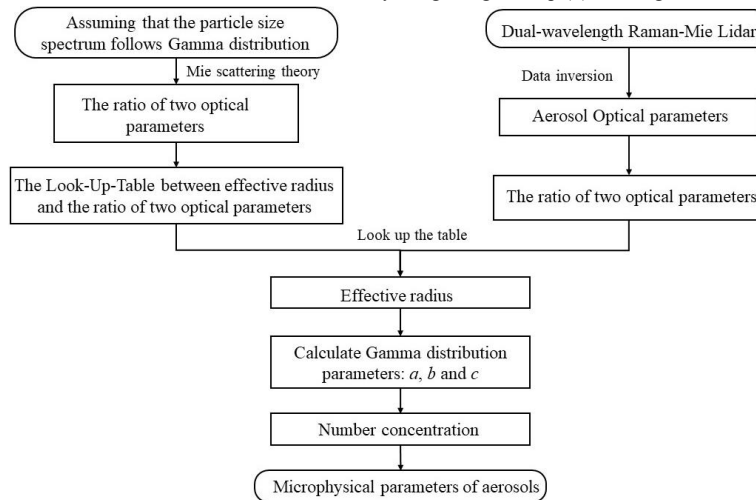
117

118 **Figure 2.** the algorithm flowchart for atmosphere particle microphysical parameters.

119 **3.2 The simulation**

120 **3.2.1 The relationship between lidar ratio, color ratio, and effective radius**

121 Due to the different complex refractive indices of aerosols and clouds, we will discuss them separately. Water clouds are

122 composed of liquid droplets, the complex refractive index of $1.33\text{-}10^{-7}i$ was selected. The theoretical relationship curves of

4

123 lidar ratio of 355 nm, lidar ratio of 532 nm, 355/1064 nm backscatter color ratio, 355/532 nm backscatter color ratio with

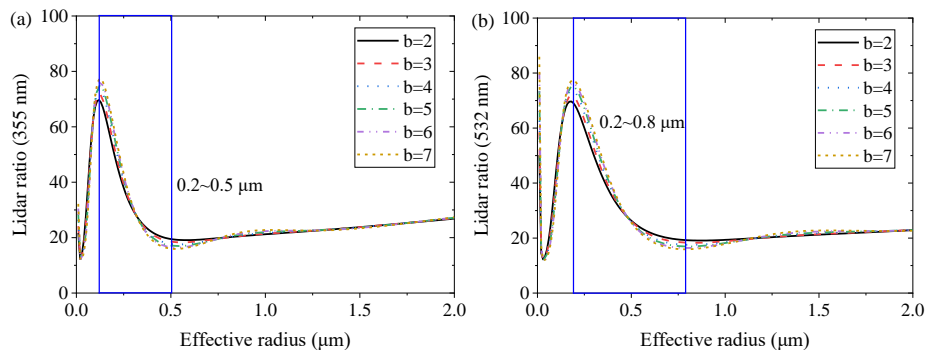124 effective radius were calculated and shown in Fig. 3(a) to 3(d).
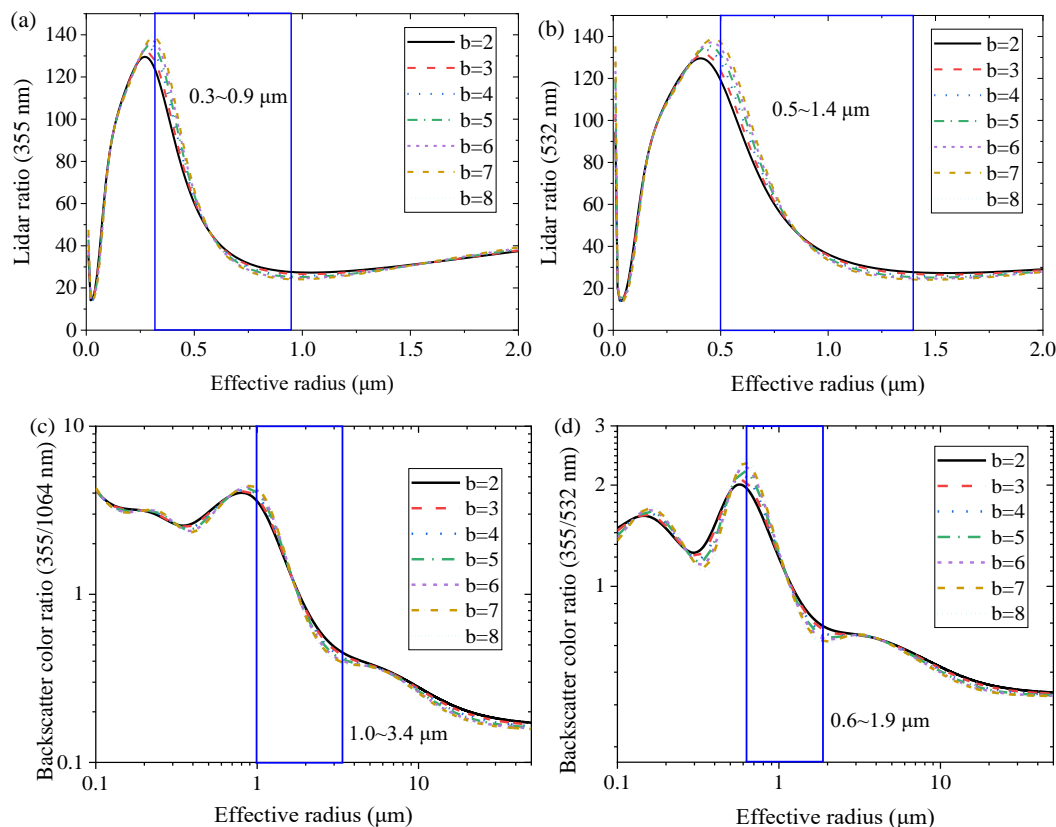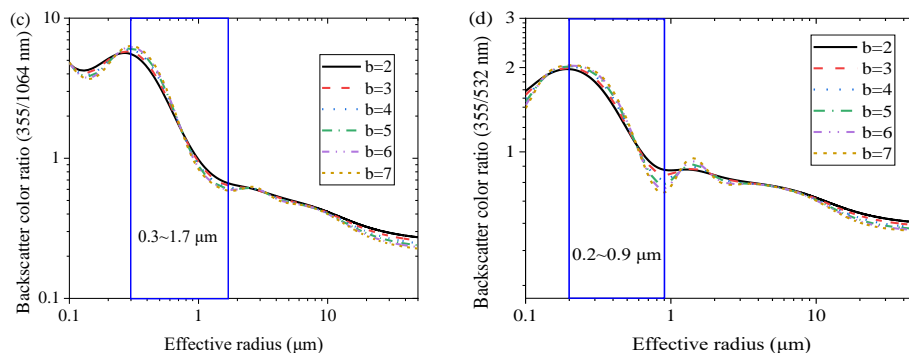
125

126

127 **Figure 3.** The theoretical relationship curves of colour ratio or lidar ratio with effective radius, *m*=1.33−0.10⁻⁷*i*. (a) Lidar ratio of 355 nm,

128 (b) lidar ratio of 532 nm, (c) the ratio of backscatter coefficients (355/1064 nm), (d) the ratio of backscatter coefficients (355/532 nm).

129 The composition of aerosols is complex, with a large variation of complex refractive index, ranging from 1.33 to 1.70 in the

130 real part and 0 to 0.05 in the imaginary part. Assuming the complex refractive index of aerosols is 1.47-0.002i, Fig. 4(a) to 4(d)

131 respectively show the theoretical relationship curves of aerosol when parameter *b* is set to 2-7.

132

133

Figure 4. The theoretical relationship curves of colour ratio or lidar ratio with effective radius, $m=1.47-0.002i$. (a) Lidar ratio of 355 nm,

(b) lidar ratio of 532 nm, (c) the ratio of backscatter coefficients (355/1064 nm), (d) the ratio of backscatter coefficients (355/532 nm).

The blue boxes in Figures 3 and 4 refer to the monotonic variation intervals of aerosols and cloud droplets, respectively. As shown in the figures, when the complex refractive index is constant and the parameter b is set to 2-7 or 2-8, the corresponding curve trend is consistent. Under a constant complex refractive index, parameter b does not change the trend of the curve. The change of b has little effect on the curve. Within the monotonic interval, the effective radius of particles can be retrieved from the curves. The monotonic interval varies with optical parameter. It can be seen that whether it is clouds or aerosols, the monotonic range of the backscatter color ratio is the widest, as shown in Fig. 3(c) and Fig. 4(c). The larger the value of b, the more pronounced the Gamma function describes the characteristics of large particles. Therefore, in the subsequent inversion, $b=6$ is taken for cloud droplets, and $b=3$ for aerosols.

Considering the laser's penetration ability, and the monotonic range of optical parameter ratios with effective radius shown in Fig. 3 and Fig. 4, the backscatter ratio of 355 nm/1064 nm for the inversion is the optimal choice. According to Fig. 3(c), the effective radius that can be retrieved using backscatter ratio of 355 nm/1064 nm is above 1 μm. The optimal inversion range is 1-3.4 μm, and the maximum inversion radius can reach 10 μm. For aerosol particles, the theoretically retrieval effective radius is above 0.3 μm, the optimal inversion interval is 0.3-1.7 μm. The above curves in Fig. 3 and Fig. 4 obtained are calculated using Mie scattering theory and are suitable for spherical particles. The spherical particles in the atmosphere can be distinguished from the depolarization ratio.

3.2.2 The influence of complex refractive index on the backscatter color ratio

When the complex refractive index changes and b is 3, the backscatter color ratios of the 355 nm and 1064 nm wavelengths are shown in Fig. 5(a) to 5(d).

154

155
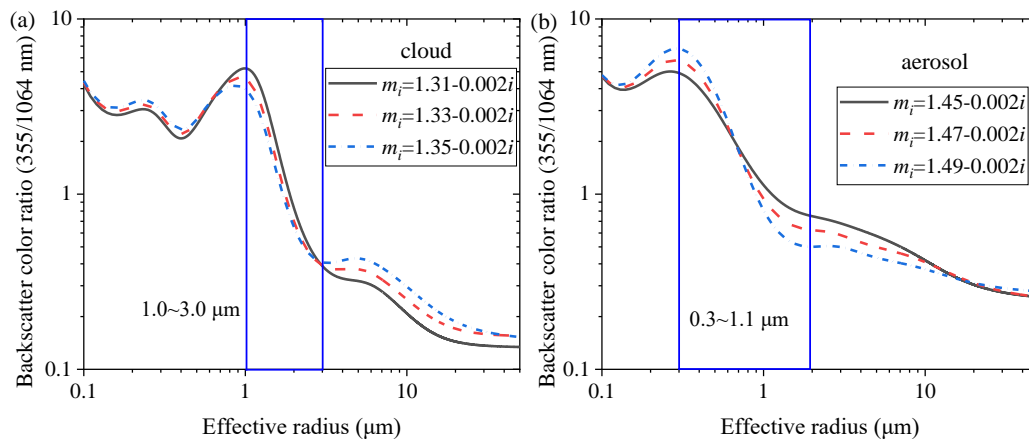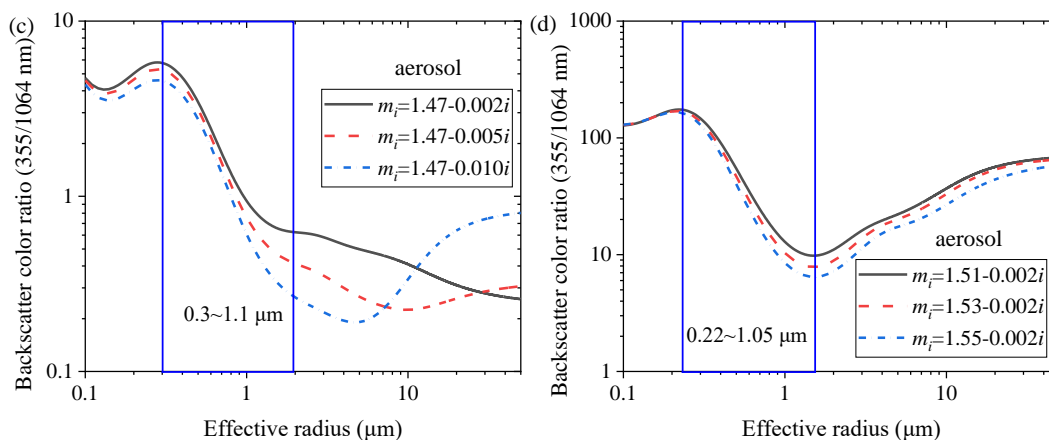
Figure 5. The color ratio with different complex refractive indices. (a)Aerosol with different real part of complex refractive index (real

157   part <1.50), (b)aerosol with different imaginary part of complex refractive index (real part <1.50), (c)aerosol with different real part of

158   complex refractive index (real part >1.50), (d)aerosol with different imaginary part of complex refractive index (real part >1.50).

159   According to Fig. 5, when the complex refractive index of particles changes, the color ratio curves will fluctuate, but they

160   always monotonically decreases at 0.3 μm to 1.7 μm. Therefore, if the aerosol composition is stable, the color ratio curve can

161   well reflect the trend of effective radius variation.

162   **3.2.3 Algorithm verification**

163   To verify the algorithm described in the above section, the APSDs and CDSDs observed by aircraft were selected for

164   simulation. The backscatter ratios of 355 nm and 1064 nm were calculated from the APSDs and CDSDs, and then, the

165   algorithm described in Section 3.1 was used to retrieve the effective radii of aerosols and cloud droplets and their number

166   concentrations. The inversion results of effective radius and number concentration, as well as their relative errors, are shown

167   in Fig.6.

168
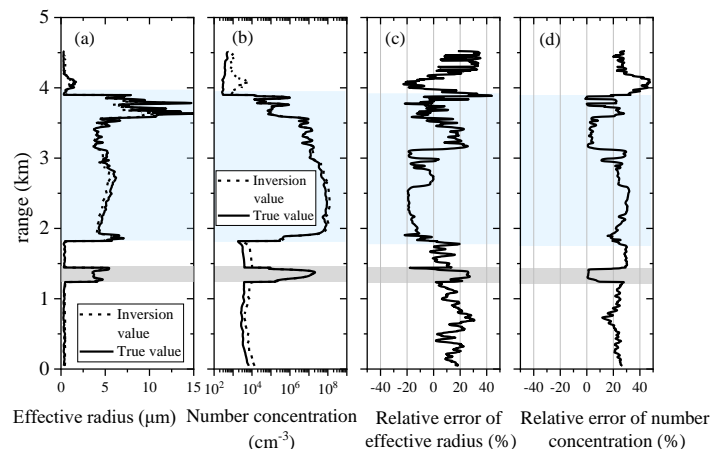
169   **Figure 6.** Simulation and verification of the algorithm with aircraft data. (a) effective radius, (b) number concentration, (c) effective radius

170   error, (d) number concentration error.

171   Figure 6(a) and 6(b) are the true values and inversion results of the effective radius and number concentration of an aircraft

172   observation at vertical altitude, respectively. Figure 6(c) and 6(d) show the relative errors, respectively. The light gray and light

173   blue shaded areas in the figures are cloud layers. It can be seen that effective radius and number concentration can be well

174   retrieved using the algorithm. Figure 6 shows that the retrieval error of cloud droplets is relatively small, within ±20% and

175   ±30% for effective radius and number concentration. The errors are ±20% and ±40% for aerosol. The inversion error of

176 microphysical parameters of aerosol particles is larger than that of cloud droplets. The reasons are: 1) aerosol types are more
177 complex, and the assumption of complex refractive index is prone to deviation; 2) APSDs is more complex than CDSDs, and
178 the adaptability to Gamma distribution is relatively low.

3.3 Error analysis of the algorithm

180   The inversion errors of effective radius and number concentration mainly come from three aspects: 1) error introduced by
181 non-spherical particles; 2) error introduced by the assumption of Gamma distribution; 3) error introduced by improper
182 assumption of complex refractive index; 4) error caused by optical parameter inversion deviation. The first three factors have
183 been discussed earlier, and this section focuses on the inversion error introduced by optical parameters. In order to
184 quantitatively analyze the impact of optical parameter errors on the effective radius inversion results, the effective radius errors
185 caused by color ratio error were calculated when they are ±5% and ±10%, and shown in Fig. 7.

186
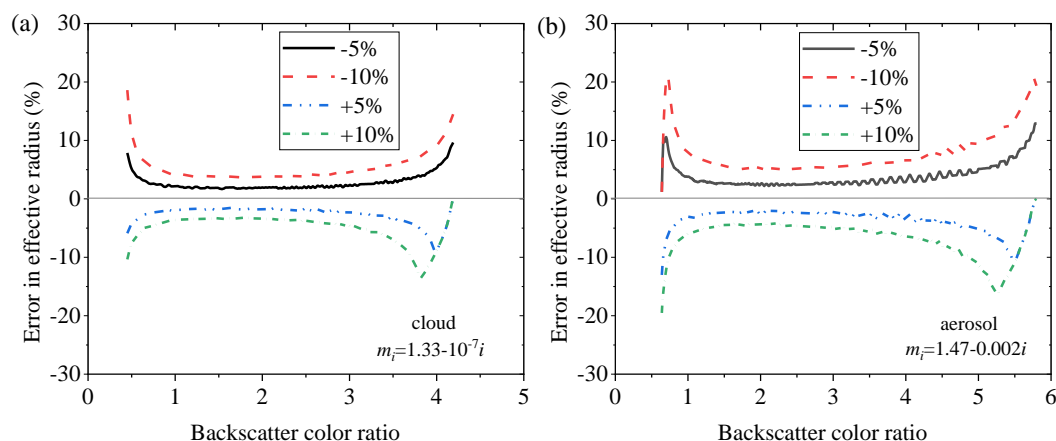
Figure 7. Errors in effective radius in Look-Up-Table when there are ±5% and ±10% errors in the backscatter color ratio. (a)Cloud
188   droplets, (b)aerosol particles.

189   From Fig. 7 (a), it can be seen that when there are errors of ±5% and ±10% in the backscatter color ratio, the inversion
190 errors of the effective radius of cloud droplets are within ±10% and ±20%, respectively. According to Fig. 7(b), when there
191 are errors of ±5% and ±10%, the inversion errors of aerosol effective radius are within ±20% and ±30%, respectively. The
192 inversion error of number concentration comes from the final superposition of optical parameter error and effective radius
193 error, and the error should be slightly larger than effective radius. In this algorithm, the complex refractive index needs to be
194 assumed. The physical and chemical properties of aerosol particles and cloud droplet particles that interact with the cloud are
195 similar, with a complex refractive index similar to that of the cloud. Continuous microphysical parameter profiles can be
196 obtained by this algorithm. For the uniformly mixed aerosol layer, it can be considered that the complex refractive index within
197 the layer remains unchanged. Therefore, this algorithm is suitable for the inversion of microphysical parameters of uniformly
198 mixed aerosol particles and small cloud droplet particles.

4 Experiment

4.1 Instrument

201   A multi-wavelength (355 nm/532 nm/1064 nm) lidar has been developed in Xi'an University of Technology (XUT). A
202 Cassegrain telescope is employed as the optical receiver, and narrowband interference filters are utilized as core filter devices
203 to finely separate the backscatter signals. The system consists of five detection channels: the two elastic scattering channels at
204 the wavelength of 355 nm and 1064 nm, the nitrogen Raman scattering channel at 387 nm, and the two polarization channels
205 at 532 nm. Table 1 summarizes the main system parameters of the lidar system.

206

Table 1. System parameters of multi-wavelength Raman-Mie scattering Lidar.

Instrument	Main instrument parameters				
Multi-wavelength Raman-Mie Scattering Lidar	Wavelength of laser	355 nm, 532 nm, 1064 nm			
	Light source	Leibao SGR series Nd: YAG pulsed laser			
		Pulse width	8.4 ns	Repetition frequency	10 Hz
		Laser divergence angle	≤ 0.5 mrad		
	Telescope	Cassegrain telescopes			
		Focal length	2 m	Field of view	0.5 mrad
		Aperture	400 mm		
	Wavelength of signal	355 nm (Mie channel), 387 nm (Raman channel), 532 nm (Polarization channel), 1064 nm (Mie channel)			
	Resolvable time	2 min			
	Minimum resolvable distance	3.75 m			

207

208   The optical parameters obtained from this system are the backscatter coefficients at 355 nm (β_{355}) and 1064 nm (β_{1064}),

209   extinction coefficient of 355nm (α_{355}), depolarization ratio of 532 nm (δ_{532}). β_{355} is obtained by inverting the Mie-scattering

210   and Raman channel without assuming lidar ratio. β_{1064} can be inverted by the Fernald method, as described in Wang et al

211   (2023a) and Li et al (2016).

212   **4.2 The experimental observation of a cloud generation process**

213   **4.2.1 The experimental observation**

214   Experimental observations were performed based on the lidar of XUT at the Jinghe National Basic Meteorological

215   Observing Station (34.43°N, 108.97°E) on September 16, 2022 (BJT). The observation experiment lasted for 7 hours with a

216   time resolution of 2 minutes. Figure 8(a) shows the Time Height Intensity (THI) of the Mie-Rayleigh signal at 1064 nm, and

217   the color bar values in the figure are the logarithm of RSCS. Figure 8(b) are the temperature and relative humidity profiles

218   obtained from the sounding balloon at 7:15 am.

219
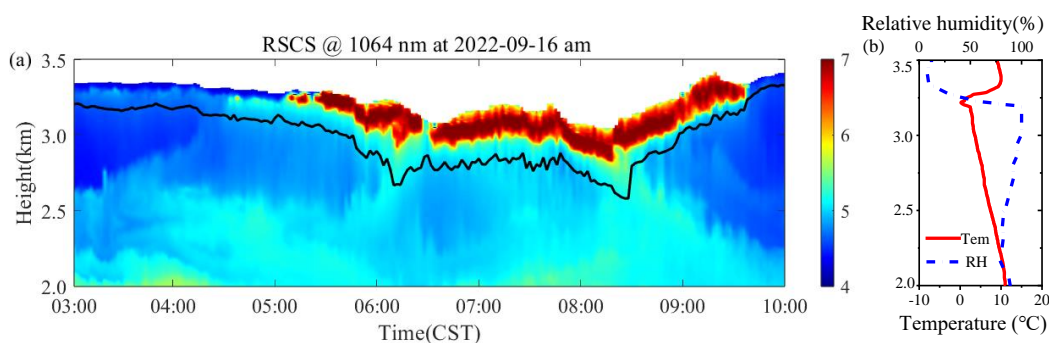
220   **Figure 8.** Lidar observations at 03:00-10:00 September 16, 2022(CST). (a) THI diagram of RSCS at 1064 nm, (b) temperature and relative

221   humidity.

222   According to Fig. 8(a), there are signals changing from weak to strong above the black curve near 3 km. After 5:00, the

223   echo signal gradually increased and the laser could not penetrate, suggesting that this should be a process of cloud formation.

224   According to the temperature and humidity profiles shown in Fig. 8(b), the temperature below 3.5 km is higher than 0℃, and

225   the relative humidity reaches over 90% at 3 km-3.2 km. Therefore, it can be determined that the strong signal appearing near

226   3 km in the atmosphere is water cloud.

227   **4.2.2 The optical and microphysical parameter profiles**

228   Figure 9 shows the observed signals of the lidar experiment near 5 o'clock on September 16, 2022, as well as the retrieved

229   optical and microphysical parameters. Figure 9(a) is the dual wavelength RSCS with enhanced signal in the cloud, especially

230   at 1064 nm. Figure 9(b) shows the volume depolarization ratio profile. The volume depolarization ratio in aerosols and clouds

231   is less than 0.05, indicating that the detected aerosols and clouds are spherical particles. Figure 9(c) show the dual wavelength

232   backscattering coefficient profiles at 355 nm and 1064 nm, while Fig. 9(d) is the ratio of backscattering coefficients at 355 nm

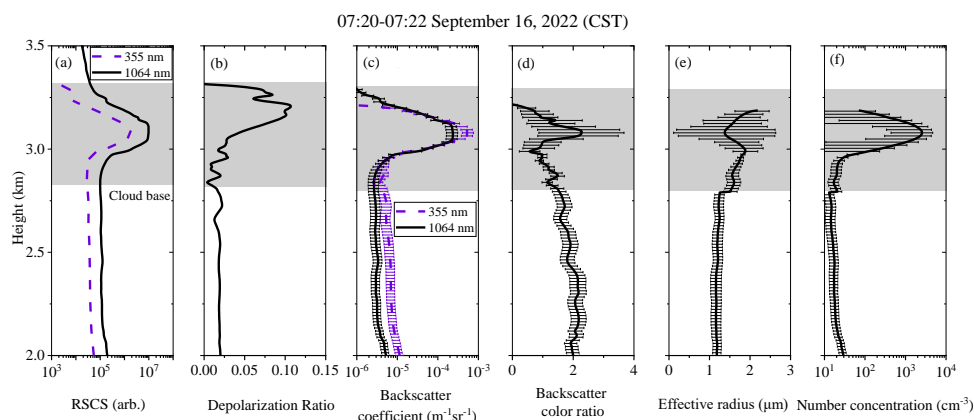233   and 1064 nm, i.e., backscatter color ratio (Wang et al., 2023b).
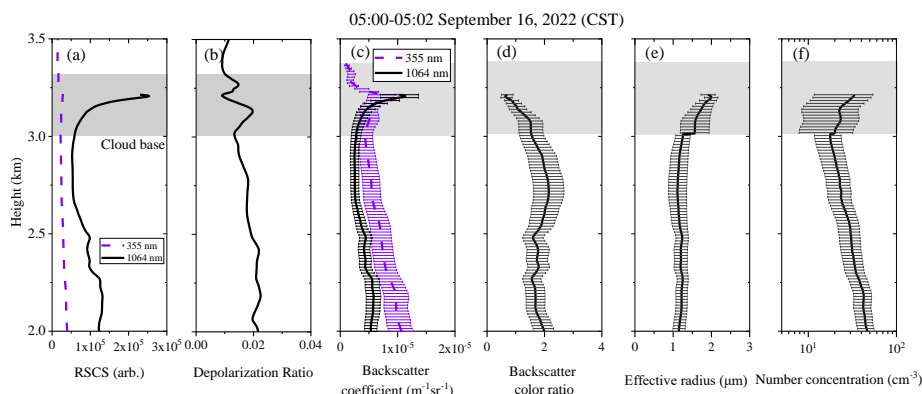
Figure 9. Lidar observation results at 05:00-05:02 September 16, 2022(CST). (a)Dual-wavelength RSCSs, (b)depolarization ratio,
(c)backscatter coefficients, (d)backscatter color ratio, (e)effective radius, (f)number concentration.

237   The depolarization ratio of aerosols below the cloud layer does not change significantly, indicating that aerosols are

238   uniformly mixed. Based on the inversion algorithm, the effective radius and number concentration profiles are calculated, as

239   shown in Fig. 9(e) and 9(f), respectively. The effective radius of aerosols under cloud layer ranges from 1.1 to 1.3 μm, and the

240   concentration fluctuates between 17 and 130 cm^{-3}, and the values decrease with increasing height. At the cloud base, the

241   effective radius reaches 1.6 μm, and the concentration is 20 cm^{-3}. As the height above the cloud base increases, the effective

242   radius and number concentration both show an increasing trend.

243   Figure 10 shows the observed signals of the lidar experiment at 7:20 on September 16, 2022, as well as the retrieved optical

244   and microphysical parameters. Compared with Figure 9, RSCS (Fig. 10(a)) and backscatter coefficients (Fig. 10(c)) in the

245   cloud layer increases significantly. From Fig. 10(b), the depolarization ratio increases above 3.2 km, and it should be caused

246   by multiple scattering or low signal-to-noise ratio. The effective radius and numerical concentration of aerosols under the

247   clouds in Fig. 10 show little change compared to Fig. 9. The number concentration in the clouds shown in Fig. 10(f) has

248   significantly increased, reaching ~2000 cm^{-3}, but the effective radius didn't change obviously, about 1-2 μm, see Fig. 10(e).


Figure 10. Lidar observation results at 07:20-07:22 September 16, 2022(CST). (a)Dual-wavelength RSCSs, (b)depolarization ratio,
(c)backscatter coefficients, (d)backscatter color ratio, (e)effective radius, (f)number concentration.

4.3 the observation results of cloud process
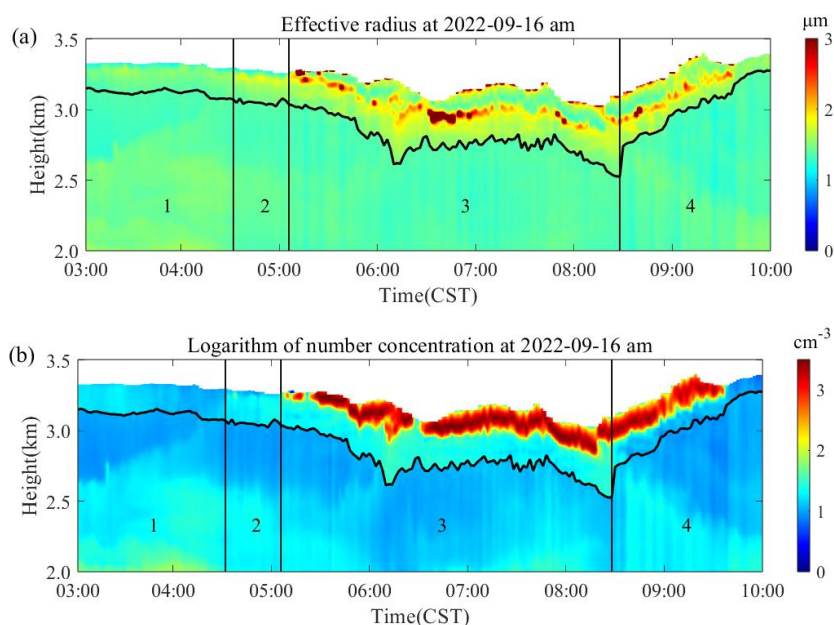
Figure 11 shows the THI of color ratio. In the region with cloud, the color ratio is relatively small, about 0.5-2, and the color ratio of aerosols is relatively large, about 2-7.
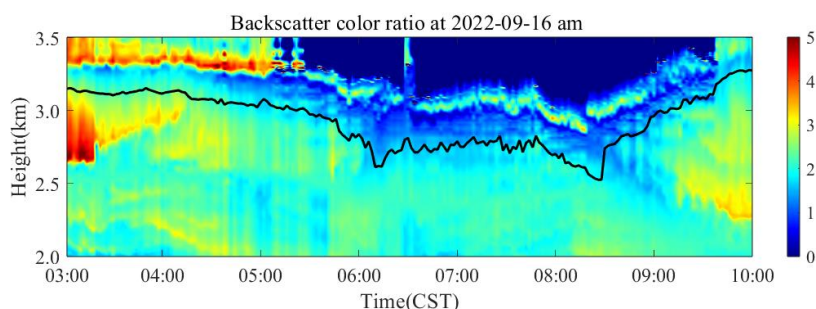
Figure 11. Inversion results of backscatter color ratio at 03:00-10:00 September 16, 2022(CST).

Figure 12. Microphysical parameters inversion results of atmospheric particulate matters at 03:00-10:00 September 16, 2022(CST). (a)Effective radius, (b)number concentration.

Figure 12 shows the changes of effective radius and particle number concentration (displayed in logarithmic form). The observation results can be separated into four stages, marked with "1/2/3/4" in Fig. 12. Stage 1: From 03:00 to 04:30, which is the early stage of cloud formation, there is an aerosol layer at 3.2 km with an average thickness of 180 m, and the effective radius and number concentration are relatively small, ranging from 1.2 to 1.5 μm and from 8.5 cm^{-3}-20.6 cm^{-3}. Stage 2: 04:30-05:06, during which the echo signal of the lidar is enhanced, the particles radius increase, and the effective radius increases to 1.4-1.8 μm. The concentration range is 13.3 cm^{-3}-25.6 cm^{-3}. Stage 3: From 05:00 to 08:30, the cloud layer thickens, the echo signal intensifies sharply, and the effective radius and number concentration increase significantly, with the effective radius of 1.5-5.3 μm and the concentration of 18.7 cm^{-3}-2853.5 cm^{-3}. Due to the increase of number concentration, the laser cannot penetrate the cloud layer. Stage 4: From 08:30 to 10:00, the cloud layer rises and the cloud base height increases from 2.5 km to 3.27 km. The effective radius inside the cloud remains unchanged, but the numerical concentration decreases. At 9:40, the cloud signal disappeared, possibly due to the cloud leaving the field of view of lidar and unable to be observed.

271 **5. Conclusion and Discussion**

272   This study proposes a method to estimate the microphysical parameters of atmosphere aerosols and small cloud droplets

273 using two optical parameters. Assuming Gamma distribution, the effective radius and number concentration of aerosols or

274 small cloud droplets can be calculated using the backscatter color ratios of 355nm and 1064nm wavelengths. An atmosphere

275 observation experiment was conducted using the multi-wavelength Lidar, and the effective radius and number concentration

276 were retrieved. The results indicate that the algorithm is stable and reliable.

277   This algorithm has simple hardware requirements for lidar, requiring only two wavelengths to achieve the retrieval of

278 microphysical parameters. At the same time, the algorithm is simple, and can obtain stable data inversion results. It is suitable

279 for the retrieval of cloud droplet generation process and aerosol with uniform mixing and relatively stable composition. The

280 limitation of this algorithm is that it requires assuming the complex refractive index of particles. The complex refractive index

281 of aerosols varies greatly, and incorrect assumptions about the complex refractive index can have a certain impact on the results.

282 Furthermore, this algorithm is not applicable for retrieval of large particle sizes (radius>10 μm). To detect larger particle sizes,

283 millimeter wave cloud radar and lidar can be used for joint observation. We will carry out this work in the future.

284 **Data availability**

285 The data and codes related to this article are available upon request from the corresponding author.

286 **Author contributions**

287 Conceptualization: Huige Di

288 Investigation: Xinhong Wang & Huige Di

289 Methodology: Huige Di & Xinhong Wang

290 Software: Xinhong Wang & Ning Chen

291 Writing — original draft: Xinhong Wang & Huige Di

292 Writing — review & editing: Huige Di, Dengxin Hua

293 Supervision: Huige Di & Jing Guo

294 Data collation: Wenhui Xin, Shichun Li, Yan Guo, Qing Yan, & Yufeng Wang

295 Project administration: Huige Di & Dengxin Hua

296 **Competing interests**

297 The authors declare that they have no conflicts of interest related to this work.

298 **Acknowledgements**

301 **Financial support**

Reference

Cai, Z. X., Li, Z. Q., Li, P. R., Li, J. X., Sun, H. P., Yang, Y. M., Gao, X., Ren, G., Ren, R. M., and Wei, J.: Vertical Distributions of Aerosol and Cloud Microphysical Properties and the Aerosol Impact on a Continental Cumulus Cloud Based on Aircraft Measurements from the Loess Plateau of China, Atmos. Environ., 270, 118888, https://doi.org/10.1016/j.atmosenv.2021.118888, 2022.

Ding, J. F., Tian, W. S., Xiao, H., Cheng, B., Liu, L., Sha, X. Z., Song, C., Sun, Y., ang Shu, W. X.: Raindrop size distribution and microphysical features of the extremely severe rainstorm on 20 July 2021 in Zhengzhou, China, Atmos. Res., 289, 106739, https://doi.org/10.1016/j.atmosres.2023.106739, 2023.

Dionisi, D., Barnaba, F., Diémoz, H., Di Liberto, L., and Gobbi, G. P.: A multiwavelength numerical model in support of quantitative retrievals of aerosol properties from automated lidar ceilometers and test applications for AOT and PM10 estimation, Atmos. Meas. Tech., 11, 6013-6042, https://doi.org/10.5194/amt-11-6013-2018, 2018.

Di, H. G., Wang, Q. Y., Hua, H. B., Li, S. W., Yan, Q., Liu, J. J., Song, Y. H., and Hua, D. X.: Aerosol Microphysical Particle Parameter Inversion and Error Analysis Based on Remote Sensing Data, Remote Sens., 10, 1753, https://doi.org/10.3390/rs10111753, 2018a.

Di, H. G., Zhao, J., Zhao, X., Zhang, Y. X., Wang, Z. X., Wang, X. W., Wang, Y. F., Zhao, H., and Hua, D.X.: Parameterization of aerosol number concentration distributions from aircraft measurements in the lower troposphere over Northern China, J. Quant. Spectrosc. Ra., 218, 46-53, https://doi.org/10.1016/j.jqsrt.2018.07.009, 2018b.

Gao, P., Wang, J., Tang, J. B., Gao, Y. Z., Liu, J. J., Yan, Q., and Hua, D. X.: Investigation of cloud droplets velocity extraction based on depth expansion and self-fusion of reconstructed hologram, Opt. Express, 30, 18713-18729, https://doi.org/10.1364/OE.458947, 2022a.

Gao, P., Wang, J., Gao, Y. Z., Liu, J. J., and Hua, D. X.: Observation on the Droplet Ranging from 2 to 16 μm in Cloud Droplet Size Distribution Based on Digital Holography, Remote Sens., 14, 2414, https://doi.org/10.3390/rs14102414, 2022b.

Hara, Y., Nishizawa, T., Sugimoto, N., Osada, K., Yumimoto, K., Uno, I., Kudo, R., and Ishimoto, H.: Retrieval of Aerosol Components Using Multi-Wavelength Mie-Raman Lidar and Comparison with Ground Aerosol Sampling, Remote Sens., 10, 937, https://doi.org/10.3390/rs10060937, 2018.

He, Y., Sun, Y. L., Wang, Q. Q., Zhou, W., Xu, W. Q., Zhang, Y. J., Xie, C. H., Zhao, J., Du, W., Qiu, Y. M., Lei, L., Fu, P. Q., Wang, Z. F., and Worsnop, D. R.: A Black Carbon-Tracer Method for Estimating Cooking Organic Aerosol from Aerosol Mass Spectrometer Measurements, Geophys. Res. Lett., 46, 8474-8483, https://doi.org/10.1029/2019GL084092, 2019.

Johnson, B. T., Christopher, S., Haywood, J. M., Osborne, S. R., McFarlane, S., Hsu, C., Salustro, C., and Kahn, R.: Measurements of aerosol properties from aircraft, satellite and ground-based remote sensing: a case-study from the Dust and Biomass burning Experiment (DABEX), Q. J. Roy. Meteor. Soc., 135, 922-934, https://doi.org/10.1002/qj.420, 2009.

Kanitz, T., Ansmann, A., Engelmann, R., and Althausen, D.: North-south cross sections of the vertical aerosol distribution over the Atlantic Ocean from multiwavelength Raman/polarization Lidar during Polarstern cruises, J. Geophys. Res.- Atmos., 118, 2643-2655, https://doi.org/10.1002/jgrd.50273, 2013.

Kaufman, Y.J., Hobbs, P.V., Kirchhoff, V.W.J.H., Artaxo, P., Remer, L.A., Holben, B.N., King, M.D., Ward, D.E., Prins, E.M., Longo, K.M., Mattos, L.F., Nobre, C.A., Spinhirne, J.D., Ji, Q., Thompson, A.M., Gleason, J.F., Christopher, S.A., and Tsay, S.-C.: Smoke, clouds, and radiation-Brazil (SCAR-B) experiment, J. Geophys. Res.-Atmos., 103, 31783-31808. https://doi.org/10.1029/98JD02281, 1998.

Kolgotin, A., Müller, D., and Romanov, A.: Particle Microphysical Parameters and the Complex Refractive Index from 3β+2α HSRL/Raman Lidar Measurements: Conditions of Accurate Retrieval, Retrieval Uncertainties and Constraints to Suppress the Uncertainties, Atmosphere-Basel, 14, 1159, https://doi.org/10.3390/atmos14071159, 2023.

345   Kulmala, M., Vehkamaki, H., Petaja, T., Maso, D. M., Lauri, A., Kerminen, V. M., Birmili, W., and McMurry, P.H.:
346   Formation and growth rates of ultrafine atmospheric particles: A review of observations, J. Aerosol Sci., 35, 143-176,
347   https://doi.org/10.1016/j.jaerosci.2003.10.003, 2004.
348   Li, L., Li, C. C., Zhao, Y. M., Li, J., and Chu, Y. Q.: Geometrical constraint experimental determination of Raman lidar
349   overlap profile, Appl. Optics, 55, 4924-4928, https://doi.org/10.1364/AO.55.004924, 2016.
350   Lohmann, U., and Feichter, J.: Global indirect aerosol effects: a review, Atmos. Chem. Phys., 5, 715-737,
351   https://doi.org/10.5194/acp-5-715-2005, 2005.
352   Martin, D. G., Apituley, A., and Donovan, P. D.: Feasibility study of integral property retrieval for tropospheric aerosol
353   from Raman lidar data using principle component analysis, Appl. Optics, 52, 2173-2186,
354   https://doi.org/10.1364/AO.52.002173, 2013.
355   Meskhidze, N., Sutherland, B., Ling, X., Dawson, K., Johnson, M. S., Henderson, B., Hostetler, C. A., Ferrare, R. A.:
356   Improving Estimates of PM2.5 Concentration and Chemical Composition by Application of High Spectral Resolution Lidar
357   (HSRL) and Creating Aerosol Types from Chemistry (CATCH) Algorithm, Atmos. Environ., 250, 118250,
358   https://doi.org/10.1016/j.atmosenv.2021.118250, 2021.
359   Miffre, A., Abou Chacra, M., Geffroy, S., Rairoux, P., Soulhac, L., Perkins, R.J., and Frejafon, E.: Aerosol load study in
360   urban area by Lidar and numerical model, Atmos. Environ., 44, 1152-1161, https://doi.org/10.1016/j.atmosenv.2009.12.031,
361   2010.
362   Moore, R. H., Wiggins, E. B., Ahern, A. T., Zimmerman, S., Montgomery, L., Campuzano Jost, P., Robinson, C. E.,
363   Ziemba, L. D., Winstead, E. L., Anderson, B. E., Brock, C. A., Brown, M. D., Chen, G., Crosbie, E. C., Guo, H., Jimenez, J.
364   L., Jordan, C. E., Lyu, M., Nault, B. A., Rothfuss, N. E., Sanchez, K. J., Schueneman, M., Shingler, T. J., Shook, M. A.,
365   Thornhill, K. L., Wagner, N. L., and Wang, J.: Sizing response of the Ultra-High Sensitivity Aerosol Spectrometer (UHSAS)
366   and Laser Aerosol Spectrometer (LAS) to changes in submicron aerosol composition and refractive index, Atmos. Meas. Tech.,
367   14, 4517-4542, https://doi.org/10.5194/amt-14-4517-2021, 2021.
368   Müller, D., Wandinger, U., and Ansmann, A.: Microphysical particle parameters from extinction and backscatter lidar
369   data by inversion with regularization: theory, Appl. Optics, 38, 2346-2357, https://doi.org/10.1364/AO.38.002346, 1999.
370   Müller, D., Hostetler, C. A., Ferrare, R. A., Burton, S. P., Chemyakin, E., Kolgotin, A., Hair, J. W., Cook, A. L., Harper,
371   D. B., Rogers, R. R., Hare, R. W., Cleckner, C. S., Obland, M. D., Tomlinson, J., Berg, L. K., and Schmid, B.: Airborne
372   Multiwavelength High Spectral Resolution Lidar (HSRL-2) observations during TCAP 2012: vertical profiles of optical and
373   microphysical properties of a smoke/urban haze plume over the northeastern coast of the US, Atmos. Meas. Tech., 7, 3487-
374   3496, https://doi.org/10.5194/amt-7-3487-2014, 2014.
375   Siomos, N., Balis, D. S., Poupkou, A., Liora, N., Dimopoulos, S., Melas, D., Giannakaki, E., Filioglou, M., Basart, S.,
376   and Chaikovsky, A.: Investigating the quality of modeled aerosol profiles based on combined lidar and sunphotometer data,
377   Atmos. Chem. Phys., 17, 7003-7023, https://doi.org/10.5194/acp-17-7003-2017, 2017.
378   Veselovskii, I., Kolgotin, A., Griaznov, V., Müller, D., Wandinger, U., and Whiteman, D. N.: Inversion with
379   regularization for the retrieval of tropospheric aerosol parameters from multiwavelength lidar sounding, Appl. Optics, 41,
380   3685-3699, https://doi.org/10.1364/AO.41.003685, 2002.
381   Veselovskii, I., Kolgotin, A., Griaznov, V., Müller, D., Franke, K., and Whiteman, David. N.: Inversion of
382   multiwavelength Raman lidar data for retrieval of bimodal aerosol size distribution, Appl. Optics, 43, 1180-1195,
383   https://doi.org/10.1364/AO.43.001180, 2004.
384   Veselovskii, I., Whiteman, D. N., Kolgotin, A., Andrews, E., and Korenskii, M.: Demonstration of aerosol property
385   profiling by multi-wavelength lidar under varying relative humidity conditions, J. Atmos. Ocean. Tech., 26, 1543-1557,
386   https://doi.org/10.1175/2009JTECHA1254.1, 2009.

387   Veselovskii, I., Dubovik, O., Kolgotin, A., Korenskiy, M., Whiteman, D. N., Allakhverdiev, K., and Huseyinoglu, F.:
388   Linear estimation of particle bulk parameters from multi-wavelength lidar measurements, Atmos. Meas. Tech., 5, 1135-1145,
389   https://doi.org/10.5194/amt-5-1135-2012, 2012.

390   Vivekanandan, J., Ghate, V. P., Jensen, J. B., Ellis, S. M., and Schwartz, M. C.: A Technique for Estimating Liquid
391   Droplet Diameter and Liquid Water Content in Stratocumulus Clouds Using Radar and Lidar Measurements, J. Atmos. Ocean.
392   Tech., 37, 2145-2161, https://doi.org/10.1175/JTECH-D-19-0092.1, 2020.

393   Wang, X. H., Di, H. G., Wang, Y. Y., Yin, Z. Z., Yuan, Y., Yang, T., Yan, Q., Li, S. C., Xin, W. H., and Hua, D. X.:
394   Correction Method of Raman Lidar Overlap Factor Based on Aerosol Optical Parameters, Acta Optica Sinica, 43, 0601005,
395   10.3788/AOS221295, 2023a.

396   Wang, X. H., Li, S. W., Hui, G. D., Li, Y., Wang, Y. Y., Yan, Q., Xin, W. H., Yuan, Y., and Hua, D. X.: Calibration
397   method of Fernald inversion for aerosol backscattering coefficient profiles via multi-wavelength Raman-Mie lidar, Opt.
398   Commun., 528, 129030, https://doi.org/10.1016/j.optcom.2022.129030, 2023b.

399   Zhao, C. F., Qiu, Y. M., Dong, X. B., Wang, Z. E., Peng, Y. R., Li, B. D., Wu, Z. H., and Wang, Y.: Negative aerosol-
400   cloud   relationship   from   aircraft   observations   over   Hebei,   China,   Earth   and   Space   Science,   5,   19-29,
401   https://doi.org/10.1002/2017EA000346, 2018.

402